nature communications

Article

https://doi.org/10.1038/s41467-024-51002-8

Ultrastrong, flexible thermogalvanic armor with a Carnot-relative efficiency over 8%

Received: 17 May 2024

Accepted: 25 July 2024

Published online: 07 August 2024

Check for updates

Jinpei Wang[1,6], Yuxin Song[2,6], Fanfei Yu[2], Yijun Zeng[1], Chenyang Wu[1], Xuezhi Qin[1], Liang Peng[1], Yitan Li[1], Yongsen Zhou[1], Ran Tao[2], Hangchen Liu[2], Hong Zhu[2], Ming Sun[2], Wanghuai Xu[3], Chao Zhang[4] ✉ & Zuankai Wang[2,5] ✉

Body heat, a clean and ubiquitous energy source, is promising as a renewable resource to supply wearable electronics. Emerging tough thermogalvanic device could be a sustainable platform to convert body heat energy into electricity for powering wearable electronics if its Carnot-relative efficiency (η_r) reaches ~5%. However, maximizing both the η_r and mechanical strength of the device are mutually exclusive. Here, we develop a rational strategy to construct a flexible thermogalvanic armor (FTGA) with a η_r over 8% near room temperature, yet preserving mechanical robustness. The key to our design lies in simultaneously realizing the thermosensitive-crystallization and salting-out effect in the elaborately designed ion-transport highway to boost η_r and improve mechanical strength. The FTGA achieves an ultrahigh η_r of 8.53%, coupling with impressive mechanical toughness of 70.65 MJ m^{-3} and substantial elongation (~900%) together. Our strategy holds sustainable potential for harvesting body heat and powering wearable electronics without recharging.

Exploring novel, efficient and sustainable waste heat utilization technologies has emerged as a global research area for energy saving and realizing carbon neutrality[1–5], as nearly 60% of the energy in the world is lost as waste heat[6]. Among them, a huge amount of waste heat is distributed near ambient temperature (classified as low-grade heat). Thermoelectric devices, such as traditional semiconductor thermoelectric generators (TEGs)[7,8] and emerging ionic thermocells (characterized by the Soret effect[9,10] or thermogalvanic effect[11–14]), which directly convert heat energy into electrical energy without any moving parts or vibration noise, offer great promise for directly powering wearable electronics. However, the effectiveness of traditional TEGs for low-grade heat conversion (i.e., body heat energy) is limited by their relatively low thermopower (Seebeck coefficient (S_e), ~μV K^{-1}), which results in a low energy conversion efficiency near ambient temperature[15,16]. Although recently developed liquid-based thermogalvanic cells (TGCs) have garnered substantial attention due to their large S_e (~mV K^{-1}) and stability, they are typically encapsulated using rigid devices and suffer from the inevitable risk of liquid leakage, which hinders their integration into wearable electronics.

Emerging flexible quasi-solid TGCs, which confine liquid electrolytes into three-dimensional gel networks, offer a possible solution to these challenges. As an important candidate to utilize body heat for powering wearable electronics directly, to realize high η_r and wearability, the thermocells must be highly efficient and mechanically robust to resist external shock. Nevertheless, state-of-the-art quasi-solid TGCs remain limited by a challenging trade-off between thermoelectric properties and mechanical strength due to the difficulty in decoupling their different requirements in material design. On the one

[1]Department of Mechanical Engineering, City University of Hong Kong, Hong Kong SAR, P. R. China. [2]Department of Mechanical Engineering, The Hong Kong Polytechnic University, Hong Kong SAR, P. R. China. [3]Department of Electrical and Electronic Engineering, The Hong Kong Polytechnic University, Hong Kong, P. R. China. [4]MOE Key Lab of Macromolecular Synthesis and Functionalization, Department of Polymer Science and Engineering, Zhejiang University, Hangzhou, P. R. China. [5]Shenzhen Research Institute of The Hong Kong Polytechnic University, Shenzhen, P. R. China. [6]These authors contributed equally: Jinpei Wang, Yuxin Song. ✉e-mail: zhangchao7@zju.edu.cn; zk.wang@polyu.edu.hk

hand, enhancing the S_e of quasi-solid TGCs can be achieved by introducing functional additives such as guanidine hydrochloride (GdmCl) to enlarge the entropy difference of redox couples in thermocells. However, these additives typically deteriorate the mechanical toughness of quasi-solid TGCs substantially due to the Hofmeister effect-induced salting-in effect, which significantly weakens the interactions of polymer chains[17,18]. Despite this, existing quasi-solid TGCs still undergo a low η_r value and could not break the bottleneck of the commercialization threshold (5%)[17,19–21]. On the other hand, improving the mechanical strength of quasi-solid TGCs can be achieved through the reinforcement of polymer networks by the design of double networks[19] or anisotropic structures via ice-template[22] or mechanical training[20,21] methods. However, these approaches often compromise the thermoelectric properties, exhibiting low output power densities and depressed η_r due to the low thermopower[19,22] or slow ionic migration speed[21] in thermocells. Therefore, effectively coupling mechanical and thermoelectric performance through a traditional single approach remains a significant challenge.

In this work, we present an ultrastrong yet flexible thermogalvanic armor (FTGA) with an ultrahigh η_r of 8.53% near room temperature through the synergy of molecular engineering and structural design, decoupling the trade-off between thermoelectric and mechanical properties in conventional quasi-solid TGCs. In contrast to conventional approaches, a novel small molecule, guanidine sulfate ($(Gdm)_2SO_4$), is first leveraged to induce thermosensitive crystallization for boosting thermopower, as well as reinforce the mechanical toughness via the Hofmeister effect[23–25]. In combination with molecular engineering, we also employ a directional freezing method to formulate the aligned channels as an "ion-transport highway" to further enhance the ion conductivity and thermopower. Our FTGA exhibits superior thermoelectric properties, including a high thermopower of 5.58 mV K^{-1}, a boosted specific output power density of 11.90 mW m^{-2} K^{-2} and a high η_r of 8.53%, as well as delivers impressive mechanical properties, such as desirable toughness of 70.65 MJ m^{-3}, high strength of 11 MPa and large elongation (~900%). To the best of our knowledge, this study pushes the boundary of the η_r of quasi-state TGCs to exceed 5%, which is much higher than the previous studies. As a proof of concept, our FTGA can be assembled into an integrated module for driving various wearable electronic devices, including an LED array and a smartwatch. We anticipate that this work will provide new insight into the design of highly efficient and flexible thermoelectric devices.

Results

Design principle

Our proposed FTGA, consisting of poly(vinyl alcohol) (PVA), $K_3Fe(CN)_6/K_4Fe(CN)_6$ and $(Gdm)_2SO_4$, is constructed by coupling molecular engineering and structural design through directional freeze-casting and subsequent salting-out processes (Fig. 1a, Supplementary Fig. 1). First, from the perspective of molecular engineering, we selected biocompatible and cost-effective PVA as a strong gel skeleton, owing to its hydrophilic and biocompatible nature[26,27], and $K_3Fe(CN)_6/K_4Fe(CN)_6$ as the redox couples because of its high intrinsic thermopower (1.4 mV K^{-1}). Distinct from most $K_3Fe(CN)_6/K_4Fe(CN)_6$-based thermocells, the biggest merit of our design is to exploit $(Gdm)_2SO_4$ as a dual molecule mediator to replace the commonly used GdmCl. In previous studies using GdmCl, Gdm^+ selectively induced $[Fe(CN)_6]^{4-}$ crystallization to enlarge the solvent-dependent entropy difference (ΔS) of $[Fe(CN)_6]^{3-}/[Fe(CN)_6]^{4-}$ (~1.7 times)[11,12] (Supplementary Fig. 2), and further enhance the thermopower. However, Gdm^+ is also a strong chaotropic cation in the Hofmeister series (Supplementary Fig. 3)[11] that can dissolve polymer chains due to the "salting-in"

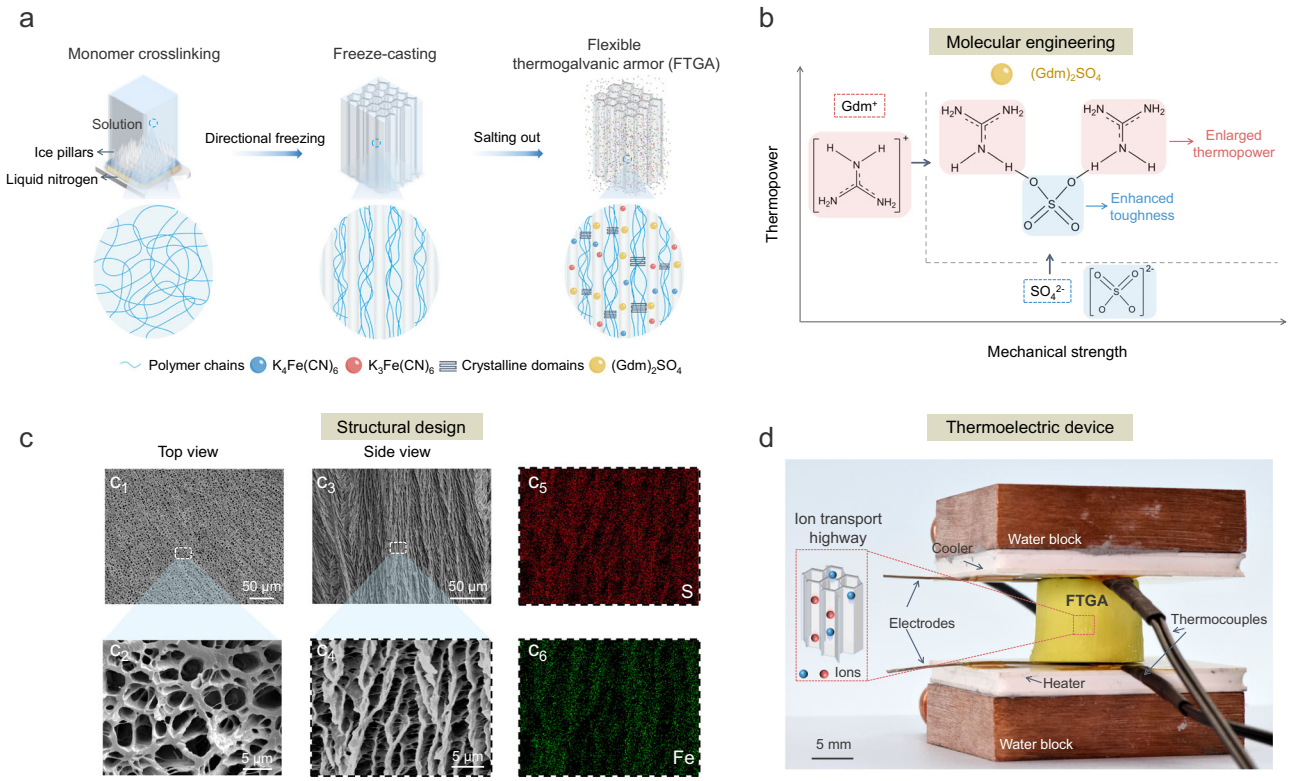

Fig. 1 | Design principle of the FTGA. a Schematic illustration of the fabrication of FTGA through the directional freezing-assisted salting-out method. **b** Mechanism illustration of guanidine sulfate to the performance of FTGA by molecular engineering. **c** SEM images showing the anisotropic structures of the FTGA. ($\mathbf{c}_1$, $\mathbf{c}_2$): top view, ($\mathbf{c}_3$, $\mathbf{c}_4$) side view, ($\mathbf{c}_5$, $\mathbf{c}_6$): energy dispersive spectrum of $\mathbf{c}_4$. The experiment was repeated three times using different samples. **d** Thermoelectric device for module electric performance measurement.

effect[28], resulting in poor mechanical properties of quasi-solid thermocells[17]. In striking contrast, $(Gdm)_2SO_4$ offers exciting ability to resolve these trade-off issues because of its unique molecular structure (Fig. 1b). For $(Gdm)_2SO_4$, besides the superiority of Gdm^+ in enhancing thermoelectric performance, its counterion, SO_4^{2-}, is a strong salting-out anion in the Hofmeister series for enhancing the mechanical properties (~2.7 times for toughness, ~1.5 times for Young's modulus, and ~1.8 times for tensile strength) (Supplementary Figs. 3 and 4). As a result, the molecular design of $(Gdm)_2SO_4$ allows the FTGA to simultaneously improve the thermopower and mechanical strength. Second, considering the structural design, the FTGA was equipped with honeycomb-like aligned channels by employing a directional freezing process (Fig. 1c_1–c_4). The aligned channels of FTGA possess intact cellular structures with compartment dimensions approximately between 1–5 μm (Fig. 1c_1, c_2), as well as highly ordered cellular arrays aligned with the ice-template direction (Fig. 1c_3, c_4). Unlike conventional isotropic gel-based thermocells (Supplementary Fig. 5), the unique aligned channels of FTGA could not only store a large number of ions (Fig. 1c_5, c_6), but also act as a "highway" for accelerating crystals sedimentation as well as ion transport, and further enhancing the thermopower (~1.4 times) and electrical conductivity (~1.3 times) (Supplementary Fig. 6). Taken together, by optimizing the synergistic effect of molecular engineering and structural design, our FTGA holds tremendous potential in attaining enhanced thermopower, improved toughness, and accelerated ion transportation, aiming at harvesting preferential energy conversion efficiency and mechanical strength.

Thermoelectric performance

We first elaborated an experimental device to evaluate the thermoelectric performance of the FTGA (Fig. 1d). In brief, the FTGA was sandwiched between two commercial platinum (Pt) wires as working electrodes, in which Pt wires are chemically inert materials that could eliminate the impact of electrode corrosion on thermopower. To measure the thermoelectric properties of the FTGA precisely, we employed a thermal stage (on the bottom) and a Peltier cooler stage (on the top) to manipulate the temperature gradient in the FTGA. When a temperature difference exists across the FTGA, the reversible reaction of the redox couples occurs on both sides, causing a potential difference in the FTGA at the two electrodes. Specifically, the oxidation reaction of $[Fe(CN)_6]^{4-}$ to $[Fe(CN)_6]^{3-}$ occurs on the hot side, releasing an electron to the electrode. This released electron is then transferred to the cold side through the external circuit and is ultimately consumed by the reduction reaction of $[Fe(CN)_6]^{3-}$ to $[Fe(CN)_6]^{4-}$. During the whole process, due to the introduction of Gdm^+ into the thermocells, the entropy difference (ΔS) of the redox couples could be enlarged, thus leading to an obvious improvement in the thermopower[29].

To demonstrate the utility of $(Gdm)_2SO_4$, we examined the influence of the concentration of $(Gdm)_2SO_4$ on the thermopower of the FTGA (Supplementary Fig. 7). With $(Gdm)_2SO_4$ concentration increasing, the S_e of the FTGA gradually increases and then drops down. When the $(Gdm)_2SO_4$ concentration is 1 M, the S_e of the FTGA reaches a peak value of 5.58 mV K^{-1}, which is 3.2 times greater than that without $(Gdm)_2SO_4$. Based on these results, we selected 1 M $(Gdm)_2SO_4$ as the optimal concentration for further characterization of the FTGA. Next, we distinguished the contributions of $(Gdm)_2SO_4$ and the aligned channels to the high thermopower of the FTGA (Fig. 2a). When only possessing aligned channels without $(Gdm)_2SO_4$, the S_e of the FTGA is significantly lower at 1.77 mV K^{-1}. For the FTGA consisting of $(Gdm)_2SO_4$ but lacking aligned channels, the S_e value is 4.07 mV K^{-1}. These results imply that the high thermopower of the FTGA originates from the synergy between $(Gdm)_2SO_4$ and the aligned channels. This synergistic effect can be further revealed by inspecting the electrical conductivity of the FTGA and control samples. Figure 2b shows that the FTGA possesses a high effective electrical conductivity of 12.98 S m^{-1}, which is much higher than the other two control samples, attributing to its aligned channels for providing a "highway" for ion transport. Furthermore, the FTGA exhibits a remarkable increase in thermopower and electrical conductivity compared to previously reported quasi-solid thermocells[17,19–22,30–37] (Fig. 2c and Supplementary Table 1), owing to the advantage of our synergetic design.

The electrical performance of the FTGA is further reflected by its output thermoelectric performance under various temperature gradients. The output voltage-current density curves and corresponding power densities of the FTGA were tested and presented in Fig. 2d, where the temperature of the cold side (T_c) was fixed at 298 K. The FTGA exhibits nearly linear voltage-current density and parabolic power density-current density relationships. For a sample with a cross-sectional area of 0.04 cm^2 and an electrode distance of 10 mm, the open-circuit voltage (V_{oc}) increases from 27 mV to 165 mV while the short-circuit current density (I_{sc}) rises from 36.73 A m^{-2} to 241.35 A m^{-2}, as ΔT increases from 5 K to 30 K. Based on these output electrical performances, the maximum output power density (P_{max}) of the FTGA is calculated. As shown in Fig. 2e, the P_{max} of the FTGA is nearly proportional to the square of ΔT, which is consistent with the theoretical result (Supplementary Note 1). Surprisingly, the normalized power density ($P_{max}/(\Delta T)^2$) of the FTGA reaches an ultrahigh level of 11.90 mW m^{-2} K^{-2}, which is 6 and 1.4 times higher than the reported state-of-the-art stretchable quasi-solid thermocells[21] and photocatalytically-enhanced aqueous thermocells[38], which have the values of 1.97 mW m^{-2} K^{-2} and 8.5 mW m^{-2} K^{-2}, respectively.

We continue to assess the output thermoelectric performance of the FTGA by figuring out the energy conversion efficiency (η) and the Carnot-relative efficiency (η_r) (Supplementary Note 2). Unlike conventional quasi-solid thermocells, our FTGA can also suppress thermal conductivity and achieve high η and η_r values. Stemming from the inhibited thermal convection caused by the crystallization of $[Fe(CN)_6]^{4-}$ and Gdm^+[39], the FTGA delivers a low effective thermal conductivity (κ_{eff}) at both parallel and perpendicular direction (relative to the aligned channels) (Supplementary Table 2). Especially, the κ_{eff} at the parallel direction is as low as 0.4434 W m^{-1} K^{-1}. Combining the merits of high thermopower, effective electrical conductivity, and low thermal conductivity, our FTGA achieves maximum η and η_r values of 0.79% and 8.53%, respectively (Fig. 2f). Notably, the η_r of FTGA largely exceeds the commercialization threshold (5%). Moreover, the η_r and $(P_{max}/(\Delta T)^2)$ values of our FTGA are much higher than those reported quasi-solid thermocells (Supplementary Fig. 9 and Table 3). These encouraging results strongly demonstrate the great potential for commercializing our FTGA in wearable electronics.

The high-output thermoelectric performance of the FTGA can be further understood from the molecular-level perspective. The thermopower of the FTGA is strongly related to the solvent-dependent entropy difference (ΔS)[29] of $[Fe(CN)_6]^{3-}/[Fe(CN)_6]^{4-}$ at the system. Owing to the higher charge density of $[Fe(CN)_6]^{4-}$ than $[Fe(CN)_6]^{3-}$, Gdm^+ could selectively induce $[Fe(CN)_6]^{4-}$ crystallization based on chaotropic-chaotropic interaction[11], so as to enlarge the ΔS of the redox ions and further enhance the S_e. This conclusion is also supported by the density functional theory (DFT) calculations (Supplementary Note 3, Supplementary Fig. 10). Before adding $(Gdm)_2SO_4$, the hydration energy of $[Fe(CN)_6]^{4-}$ and $[Fe(CN)_6]^{3-}$ is −18.71 eV and −13.24 eV, respectively, indicating that a higher charge of $[Fe(CN)_6]^{4-}$ causes a more closely packed solvation shell. After adding $(Gdm)_2SO_4$, the hydration energy of $[Fe(CN)_6]^{4-}$ is −8.86 eV, while the hydration energy of $[Fe(CN)_6]^{3-}$ is −10.45 eV. This demonstrates that more Gdm^+ incline to bond with $[Fe(CN)_6]^{4-}$ due to its higher charge, causing greater destruction of the hydration shell than $[Fe(CN)_6]^{3-}$. In contrast, $(Gdm)_2SO_4$ exhibits a slight impact on the solvation shells of $[Fe(CN)_6]^{3-}$ (Fig. 2h and Supplementary Fig. 11). This distinct change in solvation shell structure significantly increases the ΔS of $[Fe(CN)_6]^{3-}/[Fe(CN)_6]^{4-}$.

https://doi.org/10.1038/s41467-024-51002-8

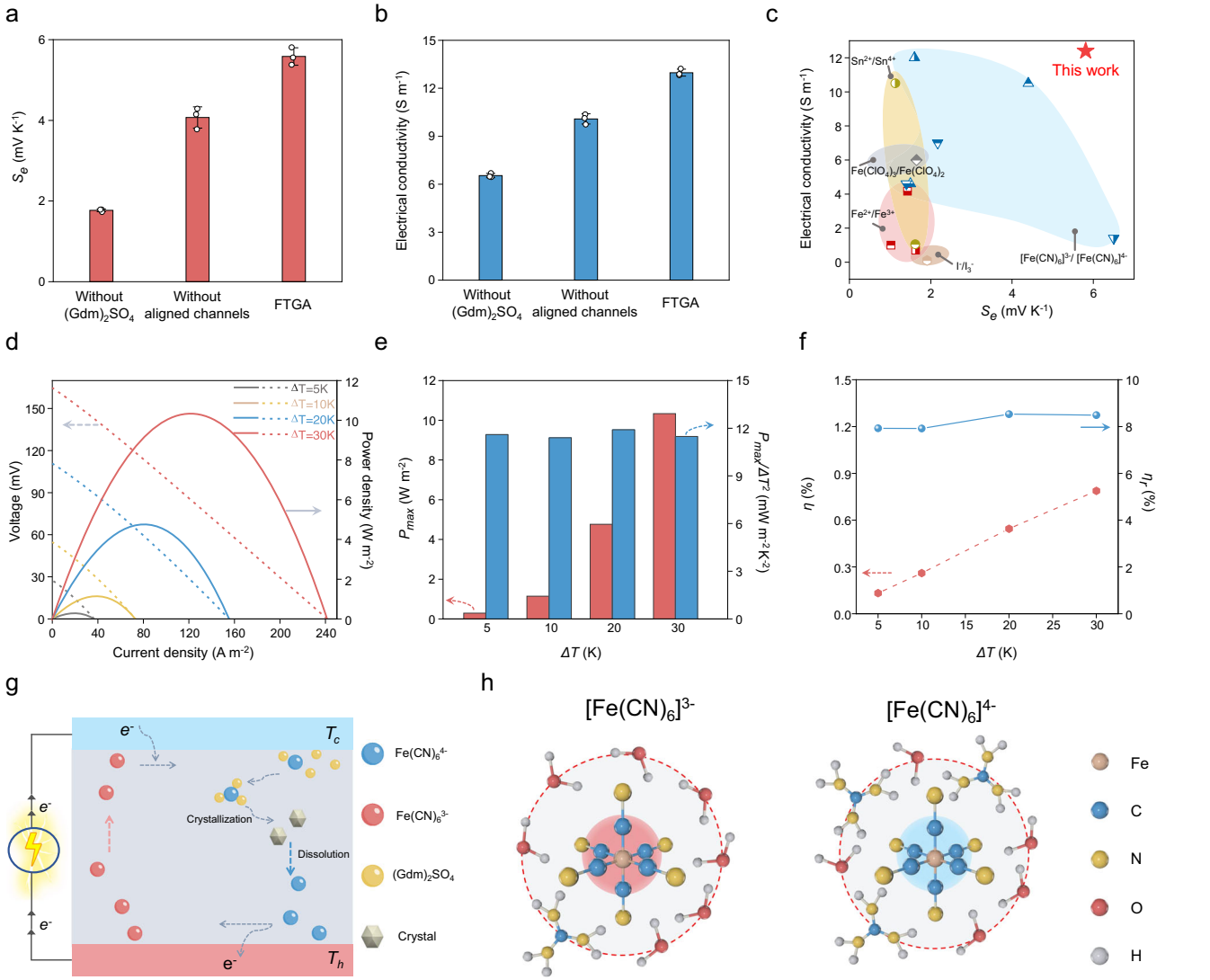

Fig. 2 | Thermoelectric output performance of the FTGA. a, **b** Optimized thermopower (S_e) (**a**) and electrical conductivity (**b**) for the FTGA induced by different structures and additive materials. Data are presented as mean values ± s.d. For the measurements of S_e and electrical conductivity, $n = 3$. **c** Property comparison of the electrical conductivity versus thermopower (S_e) for various quasi-solid thermogalvanic thermocells. **d**–**f** Output voltage-current curves and their corresponding power densities at various temperature difference (ΔT) (**d**), corresponding maximum power density (P_{max}) and specific output power density ($P_{max}/\Delta T^2$) (**e**), and thermal energy conversion efficiency (η) and the Carnot-relative efficiency (η_r) (**f**). The cold side was fixed at 298 K. **g** Working mechanism of the enhanced thermopower in FTGA system through the selective crystallization of Gdm^+ with $[Fe(CN)_6]^{4-}$. **h** Schematic solvation shell structures of $[Fe(CN)_6]^{3-}$ and $[Fe(CN)_6]^{4-}$ in FTGA.

In addition to the change in solvation shell, Gdm^+ also induces the crystallization of $[Fe(CN)_6]^{4-}$ on the cold side[11,12] of the FTGA. As this crystallization process occurs, the concentration of $[Fe(CN)_6]^{4-}$ near the cold side decreases, promoting the reduction reaction of $[Fe(CN)_6]^{3-}$ to $[Fe(CN)_6]^{4-}$. Moreover, the well-designed aligned channels can promote the formed crystals sedimenting quickly into the hot side and redissolve to generate a high concentration of $[Fe(CN)_6]^{4-}$ near the hot side, which also accelerates the oxidation reaction of $[Fe(CN)_6]^{4-}$ to $[Fe(CN)_6]^{3-}$ at the hot side and contributes to a high thermopower value.

Flexibility and mechanical toughness

In parallel with desirable thermoelectric properties, the FTGA also imparts impressive mechanical properties, which are typically not achievable with conventional quasi-solid TGCs. To highlight the significance of the synergy of molecular engineering and structural design on mechanical properties, we conducted uniaxial tensile and compressive tests to compare the mechanical behavior of different FTGA series with control samples. As depicted in Fig. 3a, our FTGA exhibits superior overall mechanical performance, with an elongation capability of ~900%, as well as high tensile strength, Young's modulus, and toughness of 11 MPa, 5.28 MPa, and 70.65 MJ m^{-3}, respectively. In contrast, the tensile strength, Young's modulus, and toughness of the sample without aligned channels are only 3.76 MPa, 2.82 MPa, and 11.4 MJ m^{-3}, respectively, while the sample without $(Gdm)_2SO_4$ has a tensile strength, Young's modulus, and toughness of 6.15 MPa, 3.56 MPa and 26.8 MJ m^{-3}, respectively (Supplementary Fig. 12). Furthermore, compared to other reported flexible TGCs, the FTGA exhibits high tensile strain and strength (Supplementary Fig. 13, Supplementary Table 4).

The superior mechanical performance of the FTGA can be further reflected by studying its mechanical behavior in the perpendicular direction relative to the aligned channels (Supplementary Fig. 14). The FTGA still exhibits an impressive elongation of ~300%, a high tensile strength of 2.41 MPa, Young's modulus of 1.42 MPa, and toughness of 5.57 MJ m^{-3}, surpassing previously reported tough quasi-state thermocells[17,19]. In addition to the tensile test, we also examined the

https://doi.org/10.1038/s41467-024-51002-8

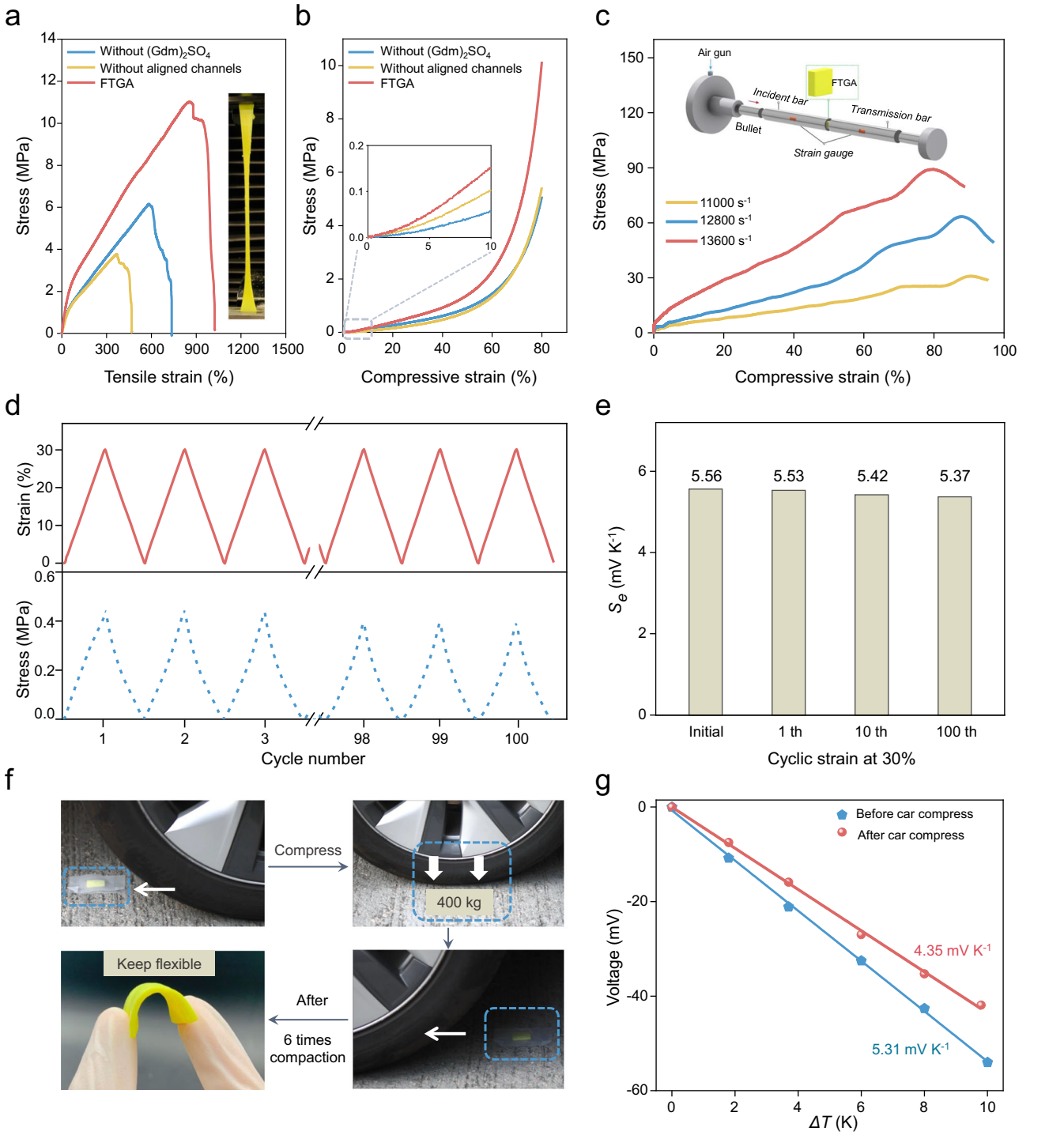

Fig. 3 | Quantitative mechanical properties and durability of FTGA. a, **b** Stress-strain curves for FTGA with different structures and additive materials from uniaxial tensile (**a**) and compressive (**b**) tests. **c** Schematic illustration of the SHPB test system (inset) and the compressive stress-strain curves of FTGA under different strain rates. **d** Cyclic stress-strain curves of the FTGA at tensile strains from 0% to 30%. **e** The variation of the thermopower (S_e) after repeated stretchable cycles. **f** Photographs of a car compression test carried out by compressing a 35 (*L*)*25 (*W*)*2 (*T*) mm (where *L* is length, *W* is width, and *T* is thickness) FTGA specimen with a 1600 kg four-wheel car. **g** Thermopower of the FTGA before and after car compression, ΔT is the temperature difference.

compressive behavior of the different series of thermocells. As shown in Fig. 3b, our FTGA could be compressed to 80% without fracturing, and its compressive stress is higher than that of the other two series of thermocells, which is consistent with the results of the tensile test. The superior mechanical properties of our FTGA could be attributed to the synergistic effects of molecular engineering and structural design. First, the directional freezing-enabled aligned channel structure can facilitate closer packing, stronger entanglement and interactions of PVA chains. Second, during the subsequent salting-out process, the presence of SO_4^{2-}, which is known as a strong salting-out anion in the Hofmeister series, effectively mitigates the negative effects of guanidine ion on the mechanical properties of the FTGA. This salting-out effect allows for efficient aggregation and crystallization of the PVA chains during this process. Therefore, the mechanical strength of the FTGA could be improved by coupling structural design and molecular engineering.

To manifest the merit of SO_4^{2-}-induced salting-out effect in strengthening mechanical strength, we inspected the mechanical properties of the FTGA with different soaking salts ($(Gdm)_2SO_4$, GdmCl). As shown in Supplementary Fig. 15, in the absence of soaking treatment, the FTGA exhibits normal elongation, tensile strength, Young's modulus, and toughness of 584%, 6.15 MPa, 3.56 MPa, and 26.8 MJ m^{-3}, respectively. However, after soaking in a GdmCl aqueous solution, the corresponding properties of the FTGA decrease to 403%, 3.31 MPa, 1.94 MPa, and 8.45 MJ m^{-3}, respectively. In contrast, when the FTGA is soaked in $(Gdm)_2SO_4$ aqueous solution with the same concentration, the corresponding properties increase to 861%, 11 MPa, 5.28 MPa, and 70.65 MJ m^{-3}, respectively. This enhanced trend enabled by $(Gdm)_2SO_4$ is also observed in the compression test (Supplementary Fig. 16). These contrasting results are attributed to the Hofmeister effect of different salts, characterized by the ability to precipitate polymer chains[25]. As the most typical chaotropic cation in the Hofmeister series, Gdm^+ directly bounds to PVA chains due to the salting-in effect, resulting in poor mechanical properties in the FTGA. In contrast, SO_4^{2-} is a strong kosmotropic anion, which can polarize hydrated water molecules and interfere with the hydrophobic hydration of macromolecule chains due to the salting-out effect, leading to the aggregation and crystallization of polymer chains and eventually enhance the mechanical properties of the FTGA.

In addition to the impressive mechanical performance under static environments, our FTGA also manifests profound application feasibility under complex, dynamic working conditions. We assessed the dynamic impact resistance of the FTGA through the split Hopkinson pressure bar (SHPB) system, which is a powerful tool for studying the behavior of materials under high-strain rate deformation[40]. As shown in Fig. 3c (Supplementary Fig. 17), the SHPB system consists of an air gun system, a bullet, an incident bar, a transmission bar and a strain gauge, in which the strain gauge on the incident bar and transmission bar could convert the mechanical wave into an electronic signal and export the stress-strain curve during the impact process. When applying different high-strain rates from 11,000 to 12,800 and 13600 s^{-1} using the SHPB system, the FTGA still demonstrates superior resistance to these dynamic high-strain impacts. Remarkably, the highest compression stress of the FTGA reaches up to ~90 MPa at the strain rate of 13,600 s^{-1}, which is a rough task for conventional hydrogels. Upon such high compression speeds, the energy absorption of the FTGA is quantified to be ~ 15.44, ~30.15, and ~46.01 MJ m^{-3} at high-strain rates of 11,000, 12,800, and 13,600 s^{-1}, respectively. The combined flexible, tough, strong and high-energy adsorption properties empower the FTGA to be a potential armored material for smart wearable electronics where involving complex, dynamic working conditions.

Durability analysis

More valuable results are obtained by further coupling the mechanical and thermoelectric properties of the FTGA. In Fig. 3d, e, we performed a cyclic stress-strain and thermoelectric test on FTGA upon tensile strains ranging from 0% to 30% in the direction perpendicular to the aligned channels, which is sufficient to accommodate the natural movements of the human body for wearable electronics[41,42]. The results reveal that the FTGA exhibits superior mechanical stability without significant hysteresis behaviour during 100 cyclic tensile strains. Furthermore, even after undergoing 100 cyclic tensile cycles, the thermopower of the FTGA remains at a high level of 5.37 mV K^{-1} (Fig. 3e), corresponding to a low attenuation of only 3.42% during repeated deformation.

The mechanical-thermoelectric properties of the FTGA can be further reflected under extreme compressive impact. A specimen with dimensions of 35 (*L*)*25 (*W*)*2 (*T*) mm was prepared for a car compression test (Fig. 3f and Supplementary Movie 1). Remarkably, even after being compressed by a car with a total weight of 1600 kg, the FTGA still keeps flexible with no fracture or irreversible deformation. Moreover, it maintains a high thermopower of 4.35 mV K^{-1} (Fig. 3g), which remains higher than many previously reported flexible quasi-state thermocells[19,20,22]. These results demonstrate the exceptional mechanical and thermoelectric stability of FTGA, further highlighting its potential for use in robust and sustainable applications such as wearable electronics.

Potential applications of FTGA device and comprehensive performance comparison

The high and stable mechanical and thermoelectric properties of the FTGA enable the exploitation of versatile, sustainable applications in wearable electronics (Fig. 4a). A key application is to serve as flexible armor that leverages the high mechanical toughness and strength of the FTGA to provide protection and enhance the durability of various devices and structures. Moreover, the FTGA is flexible and can be applied to sustainably harvest low-grade heat energy from the human body. By leveraging the temperature difference between the environment (cold source) and the human body (hot source), the FTGA can directly convert heat energy into electrical energy. This energy could then be used to power smartwatch or other wearable devices for monitoring various aspects of human health, including blood sugar levels, blood oxygen levels, heart rate, and blood pressure, etc. Such a self-powered system would enhance the convenience of human-machine interaction by eliminating the need for external power sources.

To demonstrate the scalability and practical value of the FTGA, a sizeable electronic module consisting of 36 units of the FTGA (size: 5 (*L*)*5 (*W*) *2 (*T*) mm) was designed (Supplementary Fig. 18) and prepared through a three-dimensional (3D) printing method (Supplementary Note 4). To harvest thermal energy from human body (ΔT ~ 5 K), the assembled module was tightly fixed onto a human arm through an adhesive airtight elastomer (VHB 4910, 3 M Company) (Fig. 4b), an output voltage of 0.58 V was generated, demonstrating the ability of the module to sustainably convert thermal energy into electrical energy (Fig. 4c). Furthermore, the assembled module equipped with a voltage amplifier could drive various electronic devices, including an LED array and a smartwatch (Fig. 4d, Supplementary Movie 2). These results highlight the scalability and practicality of the FTGA, demonstrating its potential for large-scale production and utilization in real-world applications, particularly in the field of energy harvesting and powering electronic devices.

Besides being used as a flexible armor for body heat harvesting and safeguarding purposes, the FTGA can also be used to combine with photovoltaic (PV) panel to achieve enhanced output performance (Supplementary Fig. 19). The PV panel can convert solar energy into electricity, however, its efficiency is largely hindered by the huge amount of heat generation during the working process. Therefore, it is important to find efficient ways to cool the device to sustain its efficiency. Interestingly, the FTGA could serve as an ideal heat sink for PV panel since it contains a lot of water, and achieve fast heat dissipation by water evaporation. Meanwhile, FTGA, itself, could generate electricity by harnessing the waste heat from the PV panel. As a proof of concept, a FTGA was attached on the back surface of the PV panel, and the surface of the PV panel was reduced ~4.3 °C during the working process (Supplementary Fig. 19a). Consequently, the output voltage of the PV panel increased by 2.14% with the assistance of FTGA (Supplementary Fig. 19b). In addition to improving the performance of PV panel, the FTGA can also utilize the temperature difference between the PV panel and the environment, further generating an output voltage of ~9.7 mV (Supplementary Fig. 19c). These results ulteriorly confirm the generality and functionality of the FTGA.

As a promising self-powered electronic device, our FTGA features high flexibility and energy conversion efficiency (Fig. 4e)[11,12,17,19–22,38,43–47]. This result indicates that our FTGA not only addresses the leakage risk

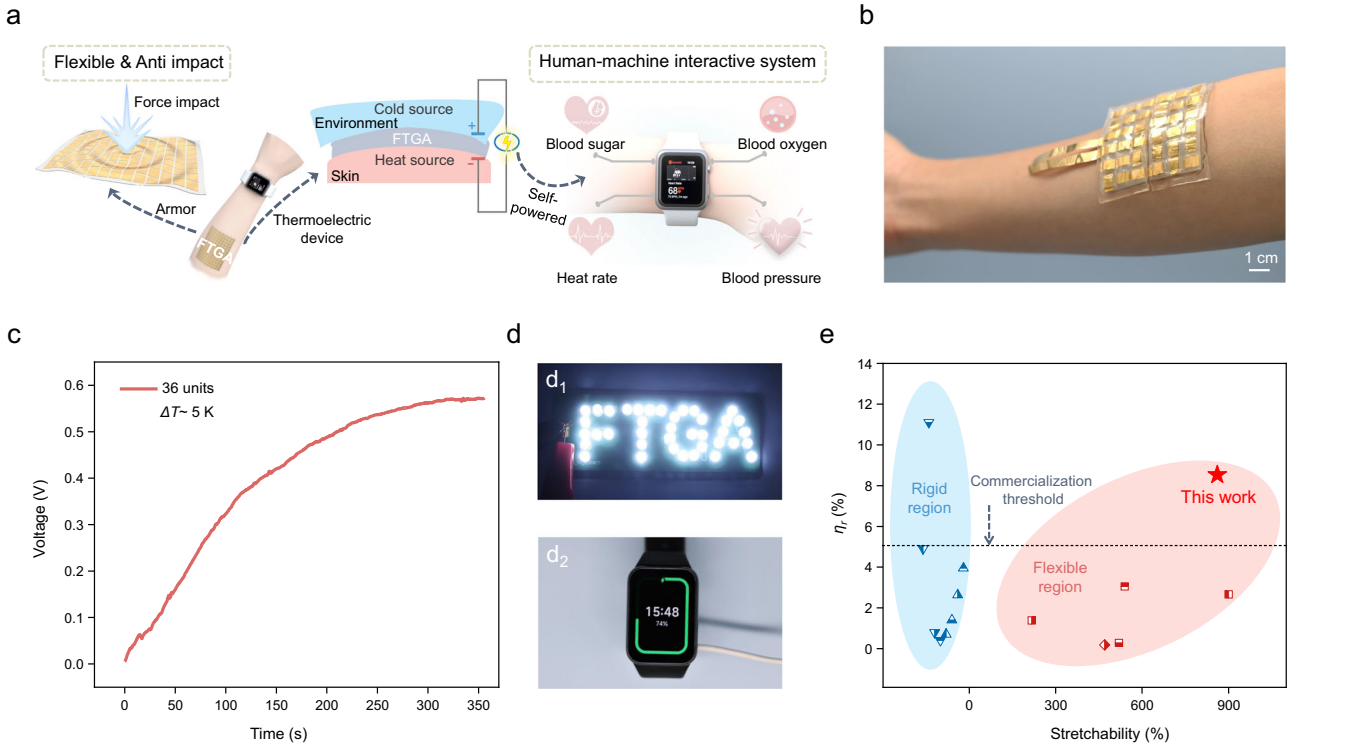

Fig. 4 | Potential application demonstration and comprehensive comparison of the FTGA. a Schematic illustration of the FTGA served as an armor for safeguarding and a flexible thermoelectric generator to power a smartwatch through harvesting thermal energy from human skin. **b** Photograph of the FTGA module fixed on a human arm for harvesting heat energy from human body. **c** The output voltage-time curve from harvesting human body heat, the temperature difference (ΔT) of the hot and cold side of the electronics was about 5 °C. **d** The FTGA module could power various electronic devices with the assistance of a passive voltage booster, including an LED array (d_1) and a smartwatch (d_2). **e** Comprehensive comparison of the Carnot-relative efficiency (η_r) versus stretchability for various thermogalvanic cells.

and rigid properties associated with liquid thermocells, but also substantially surpasses the η_r of the flexible thermocells reported in the literature and exceeds the commercialization threshold (~5%) (Supplementary Table 5), which shows a huge potential for commercial use of our device in future studies. Furthermore, our well-designed FTGA exhibits impressive comprehensive performance compared with other reported quasi-solid thermocells (Supplementary Fig. 20)[17,19–22], mainly including its Carnot-relative efficiency (η_r), electrical conductivity, thermopower (S_e), stretchability and force impact resistance properties (Supplementary Table 6). These results convincingly prove the superiority of our strategy for designing high-performance and sustainable thermogalvanic devices.

Discussion

We developed an ultrastrong, flexible thermogalvanic armor that features remarkable Carnot-relative efficiency (8.53%), specific output power density (11.90 mW m^{-2} K^{-2}), stretchability (~900%), strength (11 MPa) and toughness (70.65 MJ m^{-3}) through the integration of molecular engineering and corresponding structural design. This ingenious device overcomes the trade-off between thermoelectric and mechanical properties that exist in conventional quasi-solid thermocells, thereby offering the potential to efficiently harvest body heat for sustainably powering wearable electronics even after various mechanical deformations, including cyclic tension, car compression, and force impact. From a broader perspective, we propose that our approach may represent a paradigm shift toward enhancing the energy conversion efficiency and mechanical behavior of thermal energy harvesting systems, including quasi-solid thermocells, thermal charging cells[48], and thermal regenerative electrochemical cycles[49], etc. Based on the synergistic strategies demonstrated in this study, we anticipate significant advancements in energy harvesting and conversion from abundant and omnipresent low-grade heat.

Methods

Materials

The following materials were used: Poly(vinyl alcohol) (PVA, M_w: 146,000–168,000, 99% hydrolyzed, Sigma), Potassium ferricyanide ($K_3Fe(CN)_6$, Aladdin), Potassium ferrocyanide trihydrate ($K_4Fe(CN)_6$*$3H_2O$, Aladdin), Guanidine sulfate ($(Gdm)_2SO_4$, Aladdin), Guanidine hydrochloride (GdmCl, Aladdin), Deionized water (18.2 MΩ cm^{-1}) was obtained from a Millipore-Q system. All materials were used directly without any purification process.

Fabrication of FTGA

FTGA was fabricated through three-step procedures: (1) preparation of 10 wt.% PVA viscous solution, (2) repeated directional freezing and thawing process to form the crosslinked hydrogel network, (3) solution absorption method for redox couples and salts diffusing into hydrogel networks to form FTGA. For step (1), the PVA powders were firstly dissolved in DI water at 95 °C under vigorous stirring to form a homogeneous solution (10 wt.%). Afterward, the uniform PVA aqueous precursor was poured into a homemade mold with polytetrafluoroethylene thermal insulation and a Cu billet bottom for good thermal conduction. For step (2), the mold containing PVA solution was lowered into liquid nitrogen, where half of the Cu billet was submerged into it, and ice could nucleate and grow vertically and generate ice pillars in parallel. The directionally frozen PVA solution was then melted at room temperature. The directional freezing and thawing process was repeated for three times to form the PVA hydrogel. Finally, for step (3),

the PVA hydrogel was soaked into the solution of 0.4 M $K_3Fe(CN)_6$/$K_4Fe(CN)_6$*$3H_2O$ and different molar amounts of salts ($(Gdm)_2SO_4$) for 24 h to prepare FTGA. In this process, the ions in redox couples and salts would diffuse into gel network, and the thermopower, electrical conductivity and mechanical strength of the hydrogel could be strengthened simultaneously.

Characterization

The structures and morphology of the FTGA were characterized by environmental scanning electron microscope (FEI/Philips XL30 Esem-FEG), the samples were first soaked into deionized water for 24 h, then frozen by liquid nitrogen and freeze-dried by a freeze-dryer (LGJ-18). Voltage-time and current-voltage curves were measured by a Keithley 2400 instrument and an electrochemical station (CHI 660E), respectively. The commercial Platinum wires were used as electrodes. The thermopower measurement was illustrated in Supplementary Note 5. During the voltage and current measurements, the temperatures were controlled by a homemade setup using the TEC temperature control module (21E06), and commercial thermocouples were used to measure the temperature changes in real time too. The current-voltage curves were measured from 0 V to the open-circuit voltage and the corresponding power-current curves were calculated by the product of the corresponding current and voltage values. The effective electrical conductivity (σ_{eff}) was calculated from the slope of the current-voltage curve. The effective thermal conductivity (κ_{eff}) was measured through a thermal conductivity analyzer (TRA-4A). The tensile curves were recorded on a universal mechanical test machine (Instron 68SC-2) at room temperature. The compressive tests were conducted on a UTM system (Instron series 3382). The cyclic tensile tests were conducted by an ElectroPuls™ (Instron E1000). The Split Hopkinson pressure bar (SN-SHPB-P16) was used to test the high-velocity impact behavior of the FTGA (Supplementary Note 6).

Reporting summary

Further information on research design is available in the Nature Portfolio Reporting Summary linked to this article.

Data availability

The data for this study are available within the main text and supplementary information files. Source data are included in the source data file. Source data are provided with this paper.

References

1. Yu, B. & Duan, J. Electrochemical waste-heat harvesting. *Science* **381**, 269–270 (2023).
2. Lheritier, P. et al. Large harvested energy with non-linear pyroelectric modules. *Nature* **609**, 718–721 (2022).
3. Zhang, Y. et al. Thermal energy harvesting using pyroelectric-electrochemical coupling in ferroelectric materials. *Joule* **4**, 301–309 (2020).
4. Li, S. et al. Enhanced condensation heat transfer by water/ethanol binary liquids on polydimethylsiloxane brushes. *Droplet* **1**, 214–222 (2022).
5. Zhang, L., Shi, X.-L., Yang, Y.-L. & Chen, Z.-G. Flexible thermoelectric materials and devices: from materials to applications. *Mater. Today* **46**, 62–108 (2021).
6. Liu, C. et al. Low voltage-driven high-performance thermal switching in antiferroelectric $PbZrO_3$ thin films. *Science* **382**, 1265–1269 (2023).
7. Zhang, Q., Deng, K., Wilkens, L., Reith, H. & Nielsch, K. Micro-thermoelectric devices. *Nat. Electron.* **5**, 333–347 (2022).
8. Shi, X., Song, S., Gao, G. & Ren, Z. Global band convergence design for high-performance thermoelectric power generation in Zintls. *Science* **384**, 757–762 (2024).
9. Han, C. G. et al. Giant thermopower of ionic gelatin near room temperature. *Science* **368**, 1091–1098 (2020).
10. Li, Z. et al. Enabling giant thermopower by heterostructure engineering of hydrated vanadium pentoxide for zinc ion thermal charging cells. *Nat. Commun.* **14**, 6816 (2023).
11. Duan, J. et al. Aqueous thermogalvanic cells with a high Seebeck coefficient for low-grade heat harvest. *Nat. Commun.* **9**, 5146 (2018).
12. Yu, B. et al. Thermosensitive crystallization-boosted liquid thermocells for low-grade heat harvesting. *Science* **370**, 342–346 (2020).
13. Zhang, D. et al. Boosting thermoelectric performance of thermogalvanic hydrogels by structure engineering induced by liquid nitrogen quenching. *Adv. Energy Mater.* **14**, 2303358 (2024).
14. Wang, S. et al. High-performance cryo-temperature ionic thermoelectric liquid cell developed through a eutectic solvent strategy. *Nat. Commun.* **15**, 1172 (2024).
15. Yin, L. et al. Low-temperature sintering of Ag nanoparticles for high-performance thermoelectric module design. *Nat. Energy* **8**, 665–674 (2023).
16. Jia, B. et al. Pseudo-nanostructure and trapped-hole release induce high thermoelectric performance in PbTe. *Science* **384**, 81–86 (2024).
17. Zhang, D. et al. Stretchable thermogalvanic hydrogel thermocell with record-high specific output power density enabled by ion-induced crystallization. *Energy Environ. Sci.* **15**, 2974–2982 (2022).
18. Zhou, Y. et al. Novel porous thermosensitive gel electrolytes for wearable thermo-electrochemical cells. *Chem. Eng. J.* **449**, 137775 (2022).
19. Lei, Z., Gao, W. & Wu, P. Double-network thermocells with extraordinary toughness and boosted power density for continuous heat harvesting. *Joule* **5**, 2211–2222 (2021).
20. Lei, Z., Gao, W., Zhu, W. & Wu, P. Anti-fatigue and highly conductive thermocells for continuous electricity generation. *Adv. Funct. Mater.* **32**, 2201021 (2022).
21. Liu, L. et al. Strong tough thermogalvanic hydrogel thermocell with extraordinarily high thermoelectric performance. *Adv. Mater.* **35**, 2300696 (2023).
22. Gao, W., Lei, Z., Chen, W. & Chen, Y. Hierarchically anisotropic networks to decouple mechanical and ionic properties for high-performance quasi-solid thermocells. *ACS Nano* **16**, 8347–8357 (2022).
23. Hua, M. et al. Strong tough hydrogels via the synergy of freeze-casting and salting out. *Nature* **590**, 594–599 (2021).
24. Zhang, Y. & Cremer, P. Interactions between macromolecules and ions: the Hofmeister series. *Curr. Opin. Chem. Biol.* **10**, 658–663 (2006).
25. Jungwirth, P. & Cremer, P. S. Beyond Hofmeister. *Nat. Chem.* **6**, 261–263 (2014).
26. Zhang, H. et al. Aligned two- and three-dimensional structures by directional freezing of polymers and nanoparticles. *Nat. Mater.* **4**, 787–793 (2005).
27. Hassan, C. M. & Peppas, N. A. Structure and morphology of freeze/thawed PVA hydrogels. *Macromolecules* **33**, 2472–2479 (2000).
28. Wu, S. et al. Poly(vinyl alcohol) hydrogels with broad-range tunable mechanical properties via the Hofmeister effect. *Adv. Mater.* **33**, 2007829 (2021).
29. Sahami, S. & Weaver, M. J. Entropic and enthalpic contributions to the solvent dependence of the thermodynamics of transition-metal redox couples: part i. Couples containing ammine and ethylenediamine ligands. *J. Electroanal. Chem.* **122**, 155–170 (1981).
30. Yang, P. et al. Wearable thermocells based on gel electrolytes for the utilization of body heat. *Angew. Chem. Int. Ed.* **55**, 12050–12053 (2016).
31. Bai, C. et al. Transparent stretchable thermogalvanic PVA/gelation hydrogel electrolyte for harnessing solar energy enabled by a binary solvent strategy. *Nano Energy* **100**, 107449 (2022).

32. Peng, P. et al. Regulating thermogalvanic effect and mechanical robustness via redox ions for flexible quasi-solid-state thermocells. *Nano-Micro Lett.* **14**, 81 (2022).
33. Li, N. et al. A self-powered thermogalvanic organohydrogel-based touch-to-speech Braille transmission interface with temperature resistance and stretchability. *Compos. Sci. Technol.* **239**, 110077 (2023).
34. Wu, G., Xue, Y., Wang, L., Wang, X. & Chen, G. Flexible gel-state thermoelectrochemical materials with excellent mechanical and thermoelectric performances based on incorporating Sn^{2+}/Sn^{4+} electrolyte into polymer/carbon nanotube composites. *J. Mater. Chem. A* **6**, 3376–3380 (2018).
35. Xu, C., Sun, Y., Zhang, J., Xu, W. & Tian, H. Adaptable and wearable thermocell based on stretchable hydrogel for body heat harvesting. *Adv. Energy Mater.* **12**, 2201542 (2022).
36. Duan, J. et al. P-N conversion in thermogalvanic cells induced by thermo-sensitive nanogels for body heat harvesting. *Nano Energy* **57**, 473–479 (2019).
37. Shi, X. et al. Double hydrogen-bonding reinforced high-performance supramolecular hydrogel thermocell for self-powered sensing remote-controlled by light. *Adv. Funct. Mater.* **33**, 2211720 (2023).
38. Wang, Y. et al. In situ photocatalytically enhanced thermogalvanic cells for electricity and hydrogen production. *Science* **381**, 291–296 (2023).
39. Jin, L., Greene, G. W., MacFarlane, D. R. & Pringle, J. M. Redox-active quasi-solid-state electrolytes for thermal energy harvesting. *ACS Energy Lett.* **1**, 654–658 (2016).
40. Guan, Q. F. et al. Lightweight, tough, and sustainable cellulose nanofiber-derived bulk structural materials with low thermal expansion coefficient. *Sci. Adv.* **6**, eaaz1114 (2020).
41. Hammock, M. L., Chortos, A., Tee, B. C., Tok, J. B. & Bao, Z. 25th anniversary article: the evolution of electronic skin (e-skin): a brief history, design considerations, and recent progress. *Adv. Mater.* **25**, 5997–6038 (2013).
42. Smith, M., Cacucciolo, V. & Shea, H. Fiber pumps for wearable fluidic systems. *Science* **379**, 1327–1332 (2023).
43. Im, H. et al. High-efficiency electrochemical thermal energy harvester using carbon nanotube aerogel sheet electrodes. *Nat. Commun.* **7**, 10600 (2016).
44. Romano, M. S. et al. Carbon nanotube - reduced graphene oxide composites for thermal energy harvesting applications. *Adv. Mater.* **25**, 6602–6606 (2013).
45. Hu, R. et al. Harvesting waste thermal energy using a carbon-nanotube-based thermo-electrochemical cell. *Nano Lett.* **10**, 838–846 (2010).
46. Li, G. et al. High-efficiency cryo-thermocells assembled with anisotropic holey graphene aerogel electrodes and a eutectic redox electrolyte. *Adv. Mater.* **31**, 1901403 (2019).
47. Zhang, L. et al. High power density electrochemical thermocells for inexpensively harvesting low-grade thermal energy. *Adv. Mater.* **29**, 1605652 (2017).
48. Wang, X. et al. Direct thermal charging cell for converting low-grade heat to electricity. *Nat. Commun.* **10**, 4151 (2019).
49. Yang, Y. et al. Charging-free electrochemical system for harvesting low-grade thermal energy. *Proc. Natl Acad. Sci. USA* **111**, 17011–17016 (2014).

Acknowledgements

We acknowledge financial support from the National Natural Science Foundation of China (no. T2293694, Z.W.; no. 51975502, Z.W.; no. 52333015, Z.W.), Research Grants Council of Hong Kong (no. 11213320, Z.W.; no. SRFS2223-1S01, Z.W.; no. C6020-22G, Z.W.). We thank Prof. K. Chan, Prof. W. Gao, and Mr. Z. Lyu for their assistance in the sample tests.

Author contributions

Z.W. supervised the research. Z.W., J.W., and Y.S. conceived the research. J.W. designed the experiments. J.W. prepared the samples. J.W., Y.S., F.Y., Y.Z., C.W., and X.Q. carried out the experiments. Z.W., J.W., Y.S., F.Y., Y.Z., C.W., X.Q., L.P., Y.L., Y.Z., R.T., H.L, H.Z, M.S., W.X., and C.Z. analyzed the data. Z.W., J.W., C.Z., and Y.S. wrote the manuscript with input from the other authors.

Competing interests

The authors declare no competing interests.

Ethics statement

All experiments testing from human participants were conducted under protocols approved by the Human Subjects Ethics Sub-Committee of the Research Committee, City University of Hong Kong, with the reference number of HU-STA-00000850. The informed consent of all participants was obtained before inclusion in this study.

Additional information

Supplementary information The online version contains supplementary material available at https://doi.org/10.1038/s41467-024-51002-8.

Correspondence and requests for materials should be addressed to Chao Zhang or Zuankai Wang.

Peer review information *Nature Communications* thanks the anonymous reviewers for their contribution to the peer review of this work. A peer review file is available.